Growth and Characterization of PDMS-Stamped Halide Perovskite Single Microcrystals

Parisa Khoram[*], *Sarah Brittman*[*], *Wojciech I. Dzik*[†], *Joost N. H. Reek*[†], *and Erik C. Garnett*[*]

[*] Center for Nanophotonics, FOM Institute AMOLF, Science Park 104, 1098 XG Amsterdam, The Netherlands

[†] Homogeneous, Supramolecular & Bio-Inspired Catalysis van 't Hoff Institute for Molecular Sciences, University of Amsterdam, P.O. Box 94720, 1090 GE Amsterdam, the Netherlands

AUTHOR INFORMATION

Corresponding Author: Erik C. Garnett

Tel: +31 -20 754 7231

E-mail: garnett@amolf.nl

ABSTRACT

Recently, halide perovskites have attracted considerable attention for optoelectronic applications, but further progress in this field requires a thorough understanding of the fundamental properties of these materials. Studying perovskites in their single-crystalline form provides a model system for building such an understanding. In this work, a simple solution-processed method combined with PDMS (polydimethylsiloxane) stamping was used to prepare thin single microcrystals of halide perovskites. The method is general for a broad array of materials including $CH_3NH_3PbBr_3$, $CH_3NH_3PbCl_3$, $CH_3NH_3Pb(Br_{0.5}Cl_{0.5})_3$, $CH_3NH_3Pb(Br_{0.75}Cl_{0.25})_3$, $CsPbBr_3$, $Cs_3Bi_2Br_9$ and $Cs_3Bi_2I_9$. Electron back-scatter diffraction (EBSD) was used to investigate the microstructure of the crystals. In order to characterize the microcrystals of $CH_3NH_3PbBr_3$ electrically, the crystals were grown on pre-fabricated electrodes creating single-crystal devices contacted from the back. This back-contacted platform circumvents the incompatibility between halide perovskites and the aqueous chemistry used in standard microfabriation processes. It also allows *in situ* characterization of the perovskite crystal while it operates as a microscopic solar cell.

INTRODUCTION

Since the introduction of organolead trihalide perovskites as the light-absorbing semiconductor in solar cells,[1] much effort has been devoted to the development of these materials for optoelectronic applications.[2-5] This is due to their high efficiency and inexpensive, solution-based processing. So far the efforts in this field have led to power conversion efficiencies exceeding 20% for solar cells based on $CH_3NH_3PbI_3$.[6]

The perovskites with formula AMX_3 are crystalline materials in which A and M are cations of different sizes, and X is an anion. To date, most of the work on organic-inorganic hybrid perovskites has focused on materials with A=methylammonium ($CH_3NH_3^+$), M=lead (Pb^{2+}), and X=Cl^-, Br^-, I^-, or a mixture of these halides. Mixtures of neighboring anions (e.g. I-Br and Br-Cl) can be produced to tune the band gap from that of pure $CH_3NH_3PbI_3$ (~1.5 eV) to $CH_3NH_3PbCl_3$ (~3.1 eV).[6-8] $CH_3NH_3PbBr_3$ (~2.2 eV) sits in the middle of this range, making it and mixtures of it with $CH_3NH_3PbCl_3$ suitable for light-emission applications such as lasing[9] and light-emitting diodes (LEDs).[10-11] Mixtures of $CH_3NH_3PbBr_3$ with $CH_3NH_3PbI_3$ are appropriate for solar cells with high open-circuit voltage (V_{oc})[12-15] and the upper cell in multijunction photovoltaics. Apart from hybrid organic-inorganic perovskites, all-inorganic halide perovskites such as $CsPbBr_3$ (with a band gap of ~ 2.4 eV) have also shown promise for photovoltaics and light-emitting diodes. [16-17]

Because the microstructure and crystallinity of hybrid perovskites are known to affect their properties[18] and performance in solar cells,[19] it is important to study single crystalline perovskites free of grain boundaries.[20] Only a few previous studies have examined single crystalline hybrid perovskites.[21-29] In these works the perovskite crystals were formed by slow crystallization processes, such as antisolvent vapor-assisted crystallization,[21] top-seeded-solution-growth,[22] or solvothermal growth.[23] These processes are unlike the rapid crystallization that occurs during the drying of the spin-coated films commonly used in solar

cells. Also, the crystals' thicknesses of several millimeters were far from those relevant for optoelectronic devices. Therefore these previous studies focused primarily on the photophysical and optical properties of single crystals,[12e-12g] although Shi et al. and Dong et al. did fabricate electrodes on the top and bottom of their thick single crystals to investigate charge carrier dynamics.[12a, 12b]

Here we fabricated single-crystalline halide perovskites by applying the typical method of spincoating from solution used to make polycrystalline thin films. A PDMS-stamping step confined the solution during evaporation of the solvent and resulted in the formation of individual crystals. The typical thickness of the crystals grown by this method (~500 nm to a few μm, depending on the processing conditions) is much closer to what is commonly used in high-performance optoelectronic devices and can be reduced further to ~100 nm by adjusting the deposition conditions.[30] This method is general and can be applied to form thin single crystals of a variety of hybrid, inorganic, and lead-free halide perovskites.

EXPERIMENTAL METHODS

Preparation of methylammonium halide (CH_3NH_3X, X=Br or Cl): CH_3NH_3X was synthesized by the addition of hydrobromic acid (48% wt. in H_2O, Sigma-Aldrich) or hydrochloric acid (37% wt. in H_2O, Sigma-Aldrich) dropwise into methylamine (33% wt. in EtOH, Sigma-Aldrich) while it was stirring in an ice bath. After stirring for 2 hours in the ice bath, the solution was removed and heated to 150°C to evaporate off the solvents, while stirring was continued. The resulting powder, either white or occasionally pale yellow, was recrystallized from ethanol. The final white crystals of CH_3NH_3X were dried by heating at 100-150°C in air.

Preparation of halide perovskite solutions: All solutions were prepared at room temperature and in air. To prepare pure $CH_3NH_3PbBr_3$ crystals, $PbBr_2$ (Sigma-Aldrich, purity ≥98%) was mixed in a 1:1 molar ratio with CH_3NH_3Br in dimethylformamide (DMF) (Sigma-Aldrich,

anhydrous, 99.8%) or dimethyl sulfoxide (DMSO) (Sigma-Aldrich, anhydrous, purity≥ 99.5%). For pure $CH_3NH_3PbCl_3$ crystals, $PbCl_2$ (Sigma-Aldrich, purity ≥98%) and CH_3NH_3Cl were mixed in a 1:1 molar ratio in DMSO at 1 M concentration. To prepare mixed halide ($CH_3NH_3Pb(Br_{0.5}Cl_{0.5})_3$ and $CH_3NH_3Pb(Br_{0.75}Cl_{0.25})_3$) solutions, pure 1 M solutions of $CH_3NH_3PbBr_3$ and $CH_3NH_3PbCl_3$ in DMSO were mixed in the desired stoichiometric ratio (1:1 or 3:1). For making the all-inorganic $CsPbBr_3$ solution, CsBr (Sigma-Aldrich, 99.999%) and $PbBr_2$ precursors were mixed in a stoichiometric ratio in DMSO (0.33 M solution). $Cs_3Bi_2I_9$ and $Cs_3Bi_2Br_9$ solutions were made by mixing CsBr with $BiBr_3$ (Sigma-Aldrich, purity ≥98%) and CsI (Sigma-Aldrich, 99.9%) with BiI_3(Sigma-Aldrich, 99%) in a stoichiometric ratio in DMSO (concentrations well below 1M). The fresh solutions were ultrasonicated for 5 minutes to ensure full dissolution of the precursors prior to deposition.

Fabrication of single-crystals: The perovskite solution was spin coated on fused silica substrates. The substrates were cleaned with acetone, isopropanol, and O_2 plasma prior the deposition. A RIE/ICP plasma etcher from Oxford Instruments (Plasmalab 80 plus) was used to remove the contamination and treat the surface of the substrates. The process parameters were as follows: O_2 flow of 25 sccm, pressure of 30 mTorr, and forward power of 50 W for 2 minutes. The spinning speed and time were adjusted to prevent the full evaporation of the solvent (10 seconds at 500 rpm for DMF solutions and 30-60 s at 2000-4000 rpm for DMSO solutions). The wet substrate was immediately pressed face down onto a piece of PDMS on a hot plate held at 100°C (for DMF solutions) or 150˚C (for DMSO solutions) for 2-5 min, until the crystals formed and the substrate changed color. Inorganic perovskites in DMSO were annealed at 150-200°C. After the crystals were formed on the substrate in contact with PDMS, the sample was removed from the PDMS and annealed for about 10 min face up to ensure the evaporation of excess solvent. The PDMS stamp was fabricated by mixing the monomer and curing agent (10:1 ratio, SYLGRAD 184, Dow Corning) and curing on a piece

of clean Si wafer. The side formed in contact with the Si was always used to stamp the crystals. PDMS stamps were reused after cleaning the surface by ultrasonication in water and a rinse in isopropanol.

Back-contacted electrode fabrication: The electrodes were fabricated on glass substrates by a two-step photolithography process. Glass substrates were cleaned in acetone and isopropanol prior to spin coating with photoresist. In the first step, one set of electrodes was patterned, and the metal was deposited by electron-beam or thermal evaporation, followed by lift-off in acetone. The second lithography step was repeated as the first one, using alignment markers to adjust the gap between the electrodes. Another metal was then deposited. In the case of symmetric devices, the lithography was done in one step. The thickness of the metals was 100 nm.

Device fabrication: To make $CH_3NH_3PbBr_3$ back-contacted devices, the same procedure of spin coating the precursor solution followed by PDMS-stamping was applied using substrates with pre-fabricated electrodes. To fabricate the devices, O_2 plasma cleaning of substrates was necessary to form consistent contacts. Using a lower powered table-top plasma cleaner to prepare the electrodes resulted in inferior devices.

Atomic force microscopy: AFM images were taken by a Veeco Dimension 3100 in tapping mode.

Scanning electron microscopy: SEM images were taken by a FEI Verios 460 at 5 kV accelerating voltage, in secondary electron mode, and under a 30º tilt.

Electron Backscatter Diffraction (EBSD): The EBSD setup was built in a FEI XL30 S FEG. The patterns were collected using 20 kV accelerating voltage. The sample was tilted 70°. The patterns were indexed using Delphi 2 software from EDAX. The system was calibrated prior to indexing with Si (100).

Device Characterization: *I-V* curves were measured with an Agilent B2902A source-measure unit. To simulate solar illumination, an Oriel Sol2A Class ABA Solar Simulator from Newport was used. 1-sun intensity was calibrated using a silicon reference cell (Newport 91150V).

Scanning Photocurrent Mapping: The photocurrent maps were taken using a home-built optical setup consisting of a supercontinuum Fianium WL-SC390-3 laser, sent through an acousto-optic tunable filter (Fianium AOTF-V1-N1). The wavelength could be selected based on the experiment from 410-750 nm. The beam was focused through the objective (Mitutoyo M PLAN APO NUV 50X, NA 0.42) onto the mounted substrate. The spot radius was ~650 nm. The sample was electrically wire-bonded to a printed circuit board specially designed for the setup and scanned spatially with the focused laser beam using a piezoelectric stage (Piezosystem Jena Tritor 400 CAP). The photocurrent was measured with the same source-measure unit as used for *I-V* measurements. The voltage on the sample was scanned from zero up to 2V and then returned to zero prior to measuring the photocurrent map, and the mapping was done while the sample was kept at the short-circuit condition. The reflected beam power was measured simultaneously with a Thorlabs amplified photodiode (PDA100A) to correlate the position with the current in the superimposed maps. A silicon photodetector (Newport model 818-UV-L) was used to measure the absolute beam power in each measurement.

RESULTS AND DISCUSSION

Flat and smooth halide perovskite crystals were produced by combining solution deposition with a PDMS-stamping technique. To form the crystals, a stoichiometric solution of the perovskite precursors (CH_3NH_3Br, CH_3NH_3Cl, CsBr, or CsI and $PbBr_2$, $PbCl_2$, $BiBr_3$, or BiI_3) in dimethylformamide (DMF) or dimethyl sulfoxide (DMSO) was spin-coated onto the substrate. Prior to deposition of the solution, the substrate was cleaned with an O_2 plasma, which made it hydrophilic. Immediately after the deposition of the solution, the substrate was

pressed face down into a piece of PDMS heated on a hotplate (100-200°C) until the solvent had evaporated (Figure 1a-b). Individual crystals formed randomly on the substrate, and crystallizing in contact with the flat surface of the PDMS created faceted, smooth crystals with thicknesses of a few micrometers to hundreds of nanometers, depending on the deposition conditions (Figure 1c). If the PDMS-stamping step was not applied, rapid evaporation of the solvent in the absence of PDMS produced unshaped crystals with very rough surfaces (Figure 1d-e). Atomic force microscopy (AFM) of the surface of several $CH_3NH_3PbBr_3$ crystals indicated that the root-mean-square (rms) roughness was 7.1 ± 4.6 nm as compared to 79.1 ± 43.3 nm for crystals formed without stamping (Figure S1).

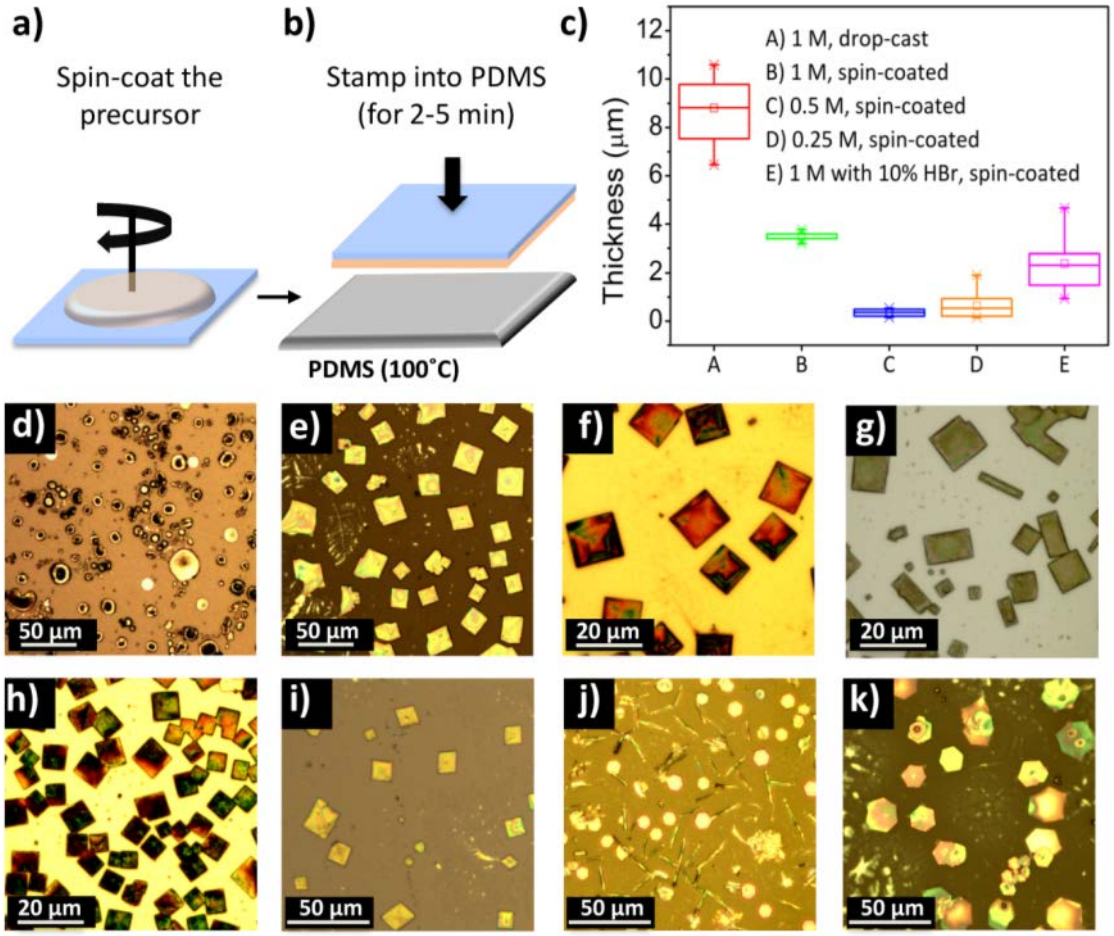

Figure 1. PDMS-stamping technique for fabrication of smooth and thin halide perovskites. (a) Spin-coating of solution on top of the prepared platform. The solvent was not allowed to

evaporate fully. (b) Pressing the substrate face down into PDMS on a hotplate (100°C) until the crystals formed. (c) Controlling the thickness of $CH_3NH_3PbBr_3$ crystals. All samples were prepared by deposition of freshly prepared $CH_3NH_3PbBr_3$ precursor solution in DMF with varied concentrations onto a glass substrate via the listed technique (drop-cast or spin-coated). For Sample E, 10 vol% of hydrobromic acid (HBr) (48% in H2O) was added to the solution. (d) Optical microscopy image of $CH_3NH_3PbBr_3$ crystals deposited by spin coating of solution on a glass substrate without PDMS-stamping. (e) Optical microscopy image of $CH_3NH_3PbBr_3$ (f) $CH_3NH_3PbCl_3$ (g) $CH_3NH_3Pb(Br_{0.75}Cl_{0.25})_3$ (h) $CH_3NH_3Pb(Br_{0.5}Cl_{0.5})_3$ (i) $CsPbBr_3$ (j) $Cs_3Bi_2Br_9$ (k) $Cs_3Bi_2I_9$ crystals fabricated by spin coating of solution on glass, followed by PDMS-stamping.

The morphology of the crystals, including their size and thickness, was influenced by several parameters, such as the concentration of the precursor solution, additives to the solution such as hydrobromic acid, and the method of deposition of the solution before stamping (e.g. drop-casting or spin-coating). The crystals, however, were not produced uniformly over the entire substrate, likely because pressure was applied non-uniformly across the substrate; therefore, in each sample at least five crystals were measured on the substrate using either a profilometer or an atomic force microscope (AFM). Because of this sampling procedure, the chart boxes that compare the thicknesses of the crystals fabricated by different parameters are not necessarily representative of the thickness variations over each substrate. In general, however, a lower concentration of solution gave a majority of thinner crystals (below 1 μm), but the lateral dimensions of the crystals decreased as well. Addition of HBr or using DMSO as the solvent[30] decreased the thickness of $CH_3NH_3PbBr_3$ crystals. Spin-coating also provided a more uniform size distribution than drop-casting.

This method is broadly applicable to produce smooth single crystals of a library of halide perovskites. In addition to crystals of $CH_3NH_3PbBr_3$, PDMS-stamped microcrystals of

$CH_3NH_3PbCl_3$ and mixed halides ($CH_3NH_3Pb(Br_{0.5}Cl_{0.5})_3$ and $CH_3NH_3Pb(Br_{0.75}Cl_{0.25})_3$) were also generated (Figure 1f-h). By varying the spin conditions and annealing temperatures, this method also produced crystals of a variety of other perovskites, including inorganic $CsPbBr_3$ and lead-free, hexagonal perovskites such as $Cs_3Bi_2I_9$ and $Cs_3Bi_2Br_9$ (Figure 1h-j).

The individual crystals of $CH_3NH_3PbBr_3$ formed by PDMS-stamping are typically single crystals with a faceted, square-prismatic shape. The smoothness of their surface allows the identification of the orientation and domains of the crystals by electron backscatter diffraction (EBSD) (Figure 2). EBSD is a SEM-based technique that is well established to determine the crystallographic orientations of microstructures.[31-32] In this technique, the focused electron beam strikes the surface of the crystal at a high angle (here, 70°). Electrons scattered from the surface form a diffraction pattern, called a Kikuchi pattern because of its prominent Kikuchi bands.[32] Several positions on the surface of each smooth crystal of $CH_3NH_3PbBr_3$ were measured (Figure 2a). The Kikuchi patterns from these positions (Figure 2b) were similar, indicating that there are no grain boundaries within the crystal. Indexing the Kikuchi patterns (Figure 2c) for fourteen different single crystals showed that the surface plane is (100) (Figure 2d). Single-crystal x-ray diffraction confirmed the single crystallinity of the square crystals (Supporting Information). Although many of the crystals formed using PDMS-stamping were square prisms, others displayed a line along their diagonal (Figure S2). EBSD patterns taken from opposite sides of the line were dissimilar, indicating that the line is a grain boundary between a <100> domain and a <110> domain. EBSD was also used to analyze the microstructure of $CsPbBr_3$ PDMS-stamped crystals, which were also typically single crystals (Supporting Information).

Optical characterization of the PDMS-stamped single crystals of $CH_3NH_3PbBr_3$ was performed by diffraction-limited absorption and photoluminescence (PL) measurements (excitation wavelength of 405 nm) (Figure 3a) on a 1-micron thick crystal. The PL spectrum,

which was collected in reflection, shows a narrow emission peak centered around 540 nm (2.29 eV). The onset of absorption is red-shifted and located at ~555 nm (2.25 eV). Controlling the thickness of the crystals allowed the measurement of the material's complex refractive index from 405-1100 nm, which agreed well with values measured on macroscopic single crystals.[30]

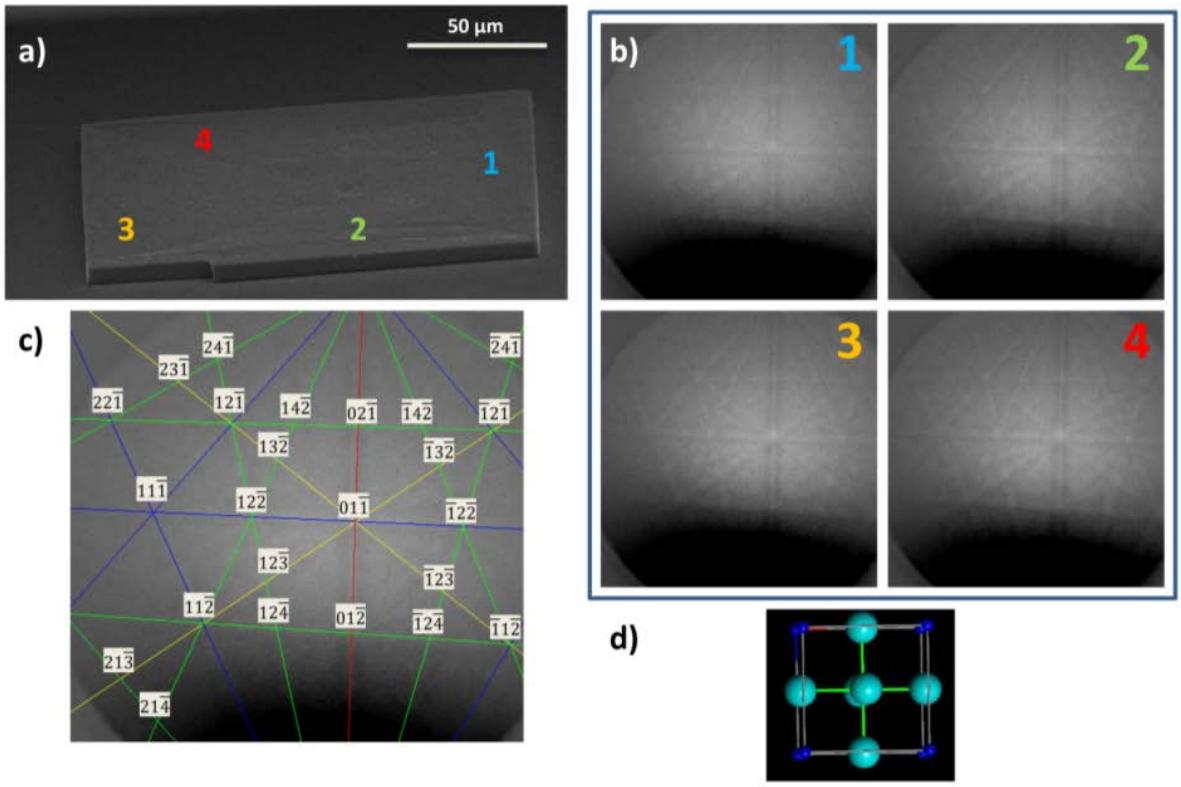

Figure 2. Electron backscatter diffraction (EBSD) of a $CH_3NH_3PbBr_3$ crystal. (a) SEM image of a $CH_3NH_3PbBr_3$ single crystal. Numbers indicate the positions of the electron beam where the EBSD patterns were collected. (b) EBSD patterns from four different locations on the crystal, which all show the same Kikuchi pattern indicating the same crystallographic orientation. Each pattern is related to the location with the similar number in figure 2a. (c) Indexed EBSD pattern. (d) The orientation of the surface of the $CH_3NH_3PbBr_3$ crystal is <100>, extracted from the indexed EBSD pattern. Green spheres are bromide anions, while blue spheres are the methylammonium cations.

To characterize the $CH_3NH_3PbBr_3$ single crystals electrically, the crystals must be contacted by metal electrodes; however, standard lithographic techniques require processing substrates in aqueous solutions, which will dissolve the ionic perovskite crystals. For this reason, electrodes were fabricated on the substrate using photolithography prior to the growth of the crystals (Supplementary Information). The first requirement for the electrodes is their appropriate energy band alignment relative to the bands of the perovskite. The valence and conduction band edges of $CH_3NH_3PbBr_3$ have been reported as 5.9 eV and 3.6 eV, respectively.[33] Based on these band positions several metals were candidates for electron- or hole-selective electrodes.[34] In the back-contacted geometry, however, the perovskite crystals are deposited on top of the electrodes, so the metals of the electrodes should be chemically inert in the solution containing the perovskite's precursors and in contact with the perovskite itself. TiO_2 is the common electron transporter material used in conventional planar perovskite solar cells,[35] therefore, titanium was a clear choice for the electron-selective contact. A thin titanium oxide layer forms on the surface of Ti metal and likely prevents any chemical reactions between the perovskite and the underlying metal. Palladium was chosen as the hole-selective contact (Figure S6), and no damage to the electrodes were observed after deposition of the crystals or during measurements. Further details regarding the selection of electrode materials are given in the Supplementary Information.

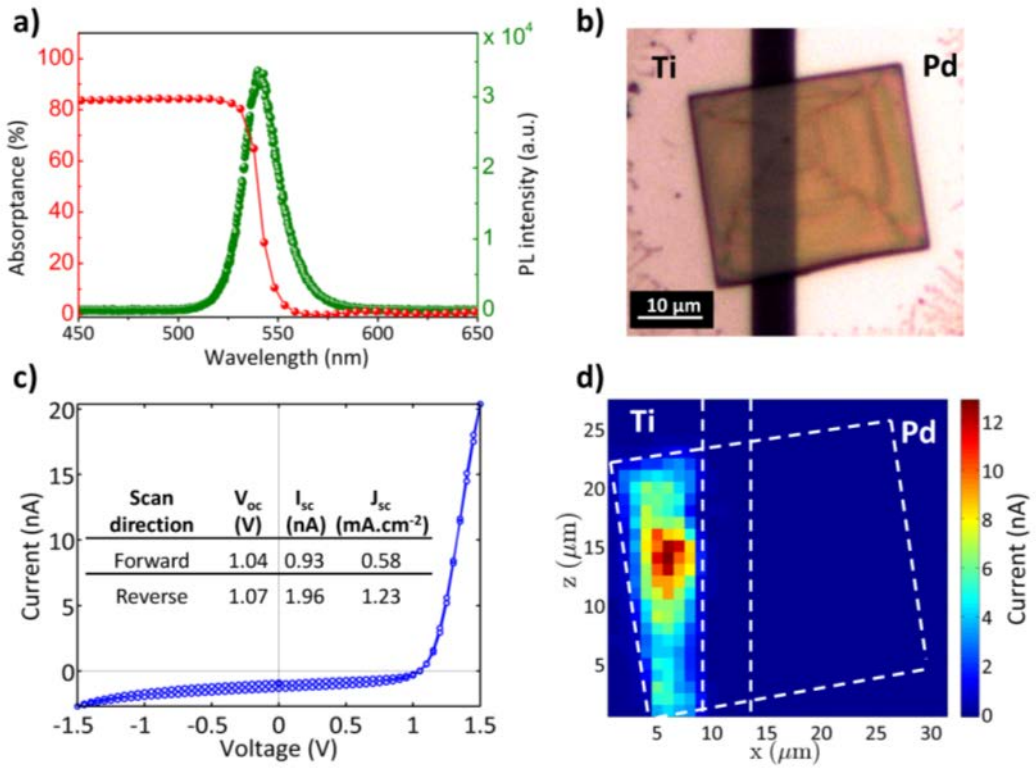

Figure 3. Optical and electrical characterization of a $CH_3NH_3PbBr_3$ single crystal. (a) Absorption (red) and photoluminescence (PL) (green) spectra of a $CH_3NH_3PbBr_3$ single crystal prepared by the PDMS-stamping technique (b) optical microscopy image of a $CH_3NH_3PbBr_3$ single crystal prepared on a pre-fabricated back-contacted electrode platform. (c) *I-V* characteristic of the $CH_3NH_3PbBr_3$ single crystal device in (b) under 1-sun illumination. Inset shows the photovoltaic performance of the device in the forward and reverse scan directions (scan rate 0.1 V/s) (d) Scanning photocurrent map of the same crystal in figure 3b (λ=540 nm, ~ 250 W cm^{-2}). Dashed lines indicate the position of the electrodes, drawn from the superimposed photocurrent map and optical image (Figure S10).

To produce solar cells, back-contacted devices with asymmetric contacts (Ti-Pd) were fabricated, followed by deposition of the perovskite crystals (Figure 3b). Current-voltage *(I-V)* curves of the devices were measured in the dark (Figure S9) and under illumination with a standard light source (AM 1.5G, 100 mW cm^{-2} irradiance) (Figure 3c). The devices displayed

rectifying *I-V* curves both in the dark and under illumination. A champion back-contacted single crystal solar cell had an open-circuit voltage (V_{oc}) of 1.04 V and 1.07 V in forward and reverse scans, respectively, better than the V_{oc} of the first demonstration of planar $CH_3NH_3PbBr_3$ perovskite solar cells in literature[14] (0.84V) but somewhat lower than cells with more optimized hole-selective layers (1.3 V)[14] and later studies (1.4V and 1.51V)[12-13]. The single crystal $CH_3NH_3PbBr_3$ solar cell exhibited a short circuit current (I_{sc}) of 0.93 nA and 1.96 nA in forward and reverse scan directions, respectively, which is equivalent to 0.58 and 1.23 mA cm^{-2} short circuit current density (J_{sc}). The J_{sc} was calculated by considering the overlapped area of the crystal with the Ti electrode as the active area, according to photocurrent mapping (Figure 3c). Again, these values are comparable to those of early planar $CH_3NH_3PbBr_3$ perovskite solar cells (1.08 mA cm^{-2})[14] although later studies[12-13] with improved hole transporter layers[13] and improving surface coverage of the $CH_3NH_3PbBr_3$[12] demonstrated much higher J_{sc} values (6.1[13] and 8.4[12] mA cm^{-2}). These reports show the importance of the hole transporter layer and suggest that the back-contacted single crystal $CH_3NH_3PbBr_3$ solar cell performance will improve substantially with deposition of proper charge transporter layers.

To investigate the spatial distribution of the photocurrent within the device, scanning photocurrent mapping using laser illumination (power density ~250 W cm^{-2} at 540 nm) was applied (Figure 3c). The positions of the crystal and electrodes were correlated to the photocurrent map by superimposing the reflectance map of the crystal taken simultaneously with the photocurrent map and the optical image (Figure S10). This correlation shows that the photocurrent originates only from the region of the crystal directly above the Ti electrode. Moreover, not all of the area above this electrode is equally active.

The observation of current localized to the electron-selective Ti contact suggests a short diffusion length for electrons in $CH_3NH_3PbBr_3$. In the case of illumination near the hole-

selective electrode, electrons must travel laterally through the width of the gap between the electrodes (few microns) to be collected by the Ti contact. If their diffusion length is shorter than this width, they recombine before being collected; therefore, regions of the crystal far from the titanium electrode appear inactive. When the crystal is illuminated near the electron-selective contact, electrons must travel only the vertical distance between their position of excitation and the electrode. Since this crystal is relatively thin (~ 1μm) and the energy of the incident photons (2.29 eV) is close to the band gap of $CH_3NH_3PbBr_3$ (~2.2 eV), some electron-hole pairs are generated close enough to the back contact for the electrons to be collected. The lack of significant lateral current decay from the edge of the electrode indicates that the carrier diffusion length is smaller than the size of the optical spot, approximately 1 μm. This short electron diffusion length is consistent with predictions of p-type conductivity in $CH_3NH_3PbBr_3$[36] and reported electron diffusion lengths in polycrystalline films of ~100 nm (in dark) and ~360 nm (under 0.03-0.04-sun illumination), which were measured by electron-beam-induced current (EBIC).[37] In millimeter-sized single crystals, Shi et al. reported much longer diffusion lengths (~3-17 μm) determined by measuring the mobility and photoluminescence lifetime of their crystals.[21] These larger crystals grown by slow precipitation over several days likely have fewer defects than the perovskite deposited by rapid precipitation after spin-coating, yielding a longer diffusion length.

The second observation in the photocurrent map of the $CH_3NH_3PbBr_3$ single crystal is the non-uniformity of the photocurrent over the Ti contact. The locations of hot spots on the photocurrent map vary for different measured crystals (Figure S11). While most of the region on the Ti electrode produces more than 3 nA of current, some regions produce as much as four times that amount. Because the photocurrent map is a convolution of light absorption and charge collection, the variations could arise from either process. For thin crystals, changes in thickness can lead to dramatic variations in photocurrent because absorption is enhanced or

suppressed by thin-film interference; however, a simple one-dimensional model (Figure S12) based on the AFM-measured thicknesses in this crystal (Figure S13) indicates that the observed variations are too large to arise from interference effects alone. Variations in the efficiency of charge collection could also contribute to this inhomogeneity and might result from a non-uniform interface between the electrode and perovskite. For example, the nucleation site of the crystal might produce the most intimate contact with the electrode, which could locally enhance the efficiency of charge collection. Differences in the thickness or chemical composition of the titanium oxide layer on the surface of the electrode could also influence the local collection efficiency and yield the observed variations in photocurrent.

CONCLUSIONS

In summary, we have introduced a simple technique to create smooth, thin halide perovskite microcrystals by combining single-step deposition of precursors from solution with PDMS-stamping. This method is general for making a variety of halide perovskites, including hybrid, all-inorganic, and lead-free hexagonal perovskites. Because of the smooth surface of the crystals, EBSD could be used to identify the microstructure of $CH_3NH_3PbBr_3$ crystals, which typically exhibited a (100) surface facet. These single crystals are ideal for studying perovskite optoelectronic devices on a fundamental level. To this end, the crystals were electrically contacted from the back to avoid any post-growth fabrication steps that might damage the crystals. We used this back-contacted platform to investigate the photovoltaic performance of single-crystal $CH_3NH_3PbBr_3$ and performed photocurrent mapping of the device to understand the spatial distribution of its photogenerated current. The photocurrent originated from the portion of the crystal directly above the electron-selective contact, suggesting these $CH_3NH_3PbBr_3$ single crystals are p-type and have an electron diffusion length below 1 μm. This PDMS-stamping approach, together with the back-contacted

platform for electrical characterization, provides a unique tool to investigate the optoelectronic properties of a variety of single-crystalline halide perovskites.

ACKNOWLEDGEMENTS

The authors thank Dr. Mark Knight and Dr. Artem Bakulin for helpful comments on the manuscript, and Andries Lof for assistance in EBSD measurements. This work is part of the research program of the Foundation for Fundamental Research on Matter (FOM), which is part of the Netherlands Organization for Scientific Research (NWO). The authors acknowledge financial support from the European Research Council under the European Union's Seventh Framework Programme (FP/2007-2013)/ERC Grant Agreement no. 337328, "NanoEnabledPV," and from an industrial partnership between Philips and FOM.

SUPPORTING INFORMATION DESCRIPTION

Morphology and EBSD of stamped $CH_3NH_3PbBr_3$ and $CsPbBr_3$ crystals, single-crystal x-ray diffraction of $CH_3NH_3PbBr_3$, fabrication of back-contacted solar cells and investigations of other metal electrodes, superimposed optical image and photocurrent map, photocurrent maps of several other single-crystal $CH_3NH_3PbBr_3$ solar cells, and model of the photocurrent in the $CH_3NH_3PbBr_3$ crystal.

AUTHOR INFORMATION

Corresponding Author E-mail: garnett@amolf.nl

Notes

The authors declare no competing financial interests.

REFERENCES

(1) Kojima, A.; Teshima, K.; Shirai, Y.; Miyasaka, T., Organometal Halide Perovskites as Visible-Light Sensitizers for Photovoltaic Cells. *J. Am. Chem. Soc.* **2009**, *131*, 6050-6051.

(2) Green, M. A.; Ho-Baillie, A.; Snaith, H. J., The Emergence of Perovskite Solar Cells. *Nat Photon* **2014**, *8*, 506-514.

(3) Snaith, H. J., Perovskites: The Emergence of a New Era for Low-Cost, High-Efficiency Solar Cells. *J. Phys. Chem. Lett.* **2013**, *4*, 3623-3630.

(4) Stranks, S. D.; Snaith, H. J., Metal-Halide Perovskites for Photovoltaic and Light-Emitting Devices. *Nat Nano* **2015**, *10*, 391-402.

(5) Brittman, S.; Adhyaksa, G. W. P.; Garnett, E. C., The Expanding World of Hybrid Perovskites: Materials Properties and Emerging Applications. *MRS Commun.* **2015**, *5*, 7-26.

(6) Jeon, N. J.; Noh, J. H.; Yang, W. S.; Kim, Y. C.; Ryu, S.; Seo, J.; Seok, S. I., Compositional Engineering of Perovskite Materials for High-Performance Solar Cells. *Nature* **2015**, *517*, 476-480.

(7) Noh, J. H.; Im, S. H.; Heo, J. H.; Mandal, T. N.; Seok, S. I., Chemical Management for Colorful, Efficient, and Stable Inorganic–Organic Hybrid Nanostructured Solar Cells. *Nano Lett.* **2013**, *13*, 1764-1769.

(8) Amat, A.; Mosconi, E.; Ronca, E.; Quarti, C.; Umari, P.; Nazeeruddin, M. K.; Grätzel, M.; De Angelis, F., Cation-Induced Band-Gap Tuning in Organohalide Perovskites: Interplay of Spin–Orbit Coupling and Octahedra Tilting. *Nano Lett.* **2014**, *14*, 3608-3616.

(9) Xing, G.; Mathews, N.; Lim, S. S.; Yantara, N.; Liu, X.; Sabba, D.; Grätzel, M.; Mhaisalkar, S.; Sum, T. C., Low-Temperature Solution-Processed Wavelength-Tunable Perovskites for Lasing. *Nat. Mater.* **2014**, *13*, 476-480.

(10) Tan, Z.-K., et al., Bright Light-Emitting Diodes Based on Organometal Halide Perovskite. *Nat. Nanotechnol.* **2014**, *9*, 687-692.

(11) Kim, Y. H.; Cho, H.; Heo, J. H.; Kim, T. S.; Myoung, N.; Lee, C. L.; Im, S. H.; Lee, T. W., Multicolored Organic/Inorganic Hybrid Perovskite Light-Emitting Diodes. *Adv. Mater.* **2015**, *27*, 1248-1254.

(12) Heo, J. H.; Song, D. H.; Im, S. H., Planar Ch3nh3pbbr3 Hybrid Solar Cells with 10.4% Power Conversion Efficiency, Fabricated by Controlled Crystallization in the Spin-Coating Process. *Adv. Mater.* **2014**, *26*, 8179-8183.

(13) Ryu, S.; Noh, J. H.; Jeon, N. J.; Kim, Y. C.; Yang, S.; Seo, J. W.; Seok, S. I., Voltage Output of Efficient Perovskite Solar Cells with High Open-Circuit Voltage and Fill Factor. *Energy Environ. Sci.* **2014**, *7*, 2614-2618.

(14) Edri, E.; Kirmayer, S.; Cahen, D.; Hodes, G., High Open-Circuit Voltage Solar Cells Based on Organic–Inorganic Lead Bromide Perovskite. *J. Phys. Chem. Lett.* **2013**, *4*, 897-902.

(15) Dymshits, A.; Rotem, A.; Etgar, L., High Voltage in Hole Conductor Free Organo Metal Halide Perovskite Solar Cells. *Journal of Materials Chemistry A* **2014**, *2*, 20776-20781.

(16) Kulbak, M.; Cahen, D.; Hodes, G., How Important Is the Organic Part of Lead Halide Perovskite Photovoltaic Cells? Efficient Cspbbr3 Cells. *J. Phys. Chem. Lett.* **2015**, *6*, 2452-2456.

(17) Yantara, N.; Bhaumik, S.; Yan, F.; Sabba, D.; Dewi, H. A.; Mathews, N.; Boix, P. P.; Demir, H. V.; Mhaisalkar, S., Inorganic Halide Perovskites for Efficient Light-Emitting Diodes. *J. Phys. Chem. Lett.* **2015**, *6*, 4360-4364.

(18) Grancini, G.; Srimath Kandada, A. R.; Frost, J. M.; Barker, A. J.; De Bastiani, M.; Gandini, M.; Marras, S.; Lanzani, G.; Walsh, A.; Petrozza, A., Role of Microstructure in the Electron–Hole Interaction of Hybrid Lead Halide Perovskites. *Nat Photon* **2015**, *9*, 695-701.

(19) Yun, J. S.; Ho-Baillie, A.; Huang, S.; Woo, S. H.; Heo, Y.; Seidel, J.; Huang, F.; Cheng, Y.-B.; Green, M. A., Benefit of Grain Boundaries in Organic–Inorganic Halide Planar Perovskite Solar Cells. *J. Phys. Chem. Lett.* **2015**, *6*, 875-880.
(20) Huang, J.; Shao, Y.; Dong, Q., Organometal Trihalide Perovskite Single Crystals: A Next Wave of Materials for 25% Efficiency Photovoltaics and Applications Beyond? *J. Phys. Chem. Lett.* **2015**, *6*, 3218-3227.
(21) Shi, D., et al., Low Trap-State Density and Long Carrier Diffusion in Organolead Trihalide Perovskite Single Crystals. *Science* **2015**, *347*, 519-522.
(22) Dong, Q.; Fang, Y.; Shao, Y.; Mulligan, P.; Qiu, J.; Cao, L.; Huang, J., Electron-Hole Diffusion Lengths > 175 Mm in Solution-Grown Ch3nh3pbi3 Single Crystals. *Science* **2015**, *347*, 967-970.
(23) Zhao, P.; Xu, J.; Dong, X.; Wang, L.; Ren, W.; Bian, L.; Chang, A., Large-Size Ch3nh3pbbr3 Single Crystal: Growth and in Situ Characterization of the Photophysics Properties. *J. Phys. Chem. Lett.* **2015**, *6*, 2622-2628.
(24) Kunugita, H., et al., Excitonic Feature in Hybrid Perovskite $Ch_3nh_3pbbr_3$ Single Crystals. *Chem. Lett.* **2015**, *44*, 852-854.
(25) Fang, H.-H.; Raissa, R.; Abdu-Aguye, M.; Adjokatse, S.; Blake, G. R.; Even, J.; Loi, M. A., Photophysics of Organic–Inorganic Hybrid Lead Iodide Perovskite Single Crystals. *Adv. Funct. Mater.* **2015**, *25*, 2378-2385.
(26) Yamada, Y.; Yamada, T.; Phuong, L. Q.; Maruyama, N.; Nishimura, H.; Wakamiya, A.; Murata, Y.; Kanemitsu, Y., Dynamic Optical Properties of Ch3nh3pbi3 Single Crystals as Revealed by One- and Two-Photon Excited Photoluminescence Measurements. *J. Am. Chem. Soc.* **2015**, *137*, 10456-10459.
(27) Grancini, G.; D'Innocenzo, V.; Dohner, E. R.; Martino, N.; Srimath Kandada, A. R.; Mosconi, E.; De Angelis, F.; Karunadasa, H. I.; Hoke, E. T.; Petrozza, A., Ch3nh3pbi3 Perovskite Single Crystals: Surface Photophysics and Their Interaction with the Environment. *Chemical Science* **2015**, *6*, 7305-7310.
(28) Yang, Y.; Yan, Y.; Yang, M.; Choi, S.; Zhu, K.; Luther, J. M.; Beard, M. C., Low Surface Recombination Velocity in Solution-Grown Ch3nh3pbbr3 Perovskite Single Crystal. *Nat Commun* **2015**, *6*, 7961-7966.
(29) Zhang, T.; Yang, M.; Benson, E. E.; Li, Z.; van de Lagemaat, J.; Luther, J. M.; Yan, Y.; Zhu, K.; Zhao, Y., A Facile Solvothermal Growth of Single Crystal Mixed Halide Perovskite Ch3nh3pb(Br1-Xclx)3. *Chem. Commun.* **2015**, *51*, 7820-7823.
(30) Brittman, S.; Garnett, E. C., Measuringnandkat the Microscale in Single Crystals of Ch3nh3pbbr3perovskite. *The Journal of Physical Chemistry C* **2016**, *120*, 616-620.
(31) Dingley, D. J.; Randle, V., Microtexture Determination by Electron Back-Scatter Diffraction. *Journal of Materials Science* **1992**, *27*, 4545-4566.
(32) Schwartz, A. J.; Kumar, M.; Adams, B. L.; Field, D. P., *Electron Backscatter Diffraction in Materials Science*; Springer: New York, 2009; Vol. 2.
(33) Schulz, P.; Edri, E.; Kirmayer, S.; Hodes, G.; Cahen, D.; Kahn, A., Interface Energetics in Organo-Metal Halide Perovskite-Based Photovoltaic Cells. *Energy Environ. Sci.* **2014**, *7*, 1377-1381.
(34) Goldmann, A.; Landolt, H.; Börnstein, R., *Electronic Structure of Solids: Photoemission Spectra and Related Data*; Springer: New York, 1994.
(35) Chueh, C.-C.; Li, C.-Z.; Jen, A. K. Y., Recent Progress and Perspective in Solution-Processed Interfacial Materials for Efficient and Stable Polymer and Organometal Perovskite Solar Cells. *Energy Environ. Sci.* **2015**, *8*, 1160-1189.
(36) Shi, T.; Yin, W.-J.; Hong, F.; Zhu, K.; Yan, Y., Unipolar Self-Doping Behavior in Perovskite Ch3nh3pbbr3. *Appl. Phys. Lett.* **2015**, *106*, 103902.

(37) Kedem, N.; Brenner, T. M.; Kulbak, M.; Schaefer, N.; Levcenko, S.; Levine, I.; Abou-Ras, D.; Hodes, G.; Cahen, D., Light-Induced Increase of Electron Diffusion Length in a P–N Junction Type Ch3nh3pbbr3 Perovskite Solar Cell. *J. Phys. Chem. Lett.* **2015**, *6*, 2469-2476.

Table of Contents graphic

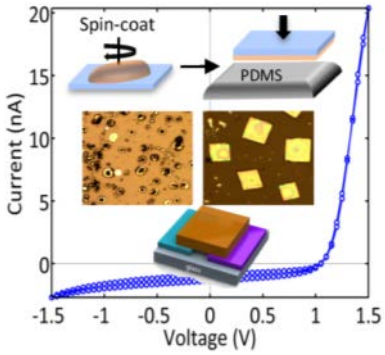

Growth and Characterization of PDMS-Stamped Halide Perovskite Single Microcrystals

Parisa Khoram*, Sarah Brittman*, Wojciech I. Dzik†, Joost N. H. Reek†, and Erik C. Garnett*

* Center for Nanophotonics, FOM Institute AMOLF, Science Park 104, 1098 XG Amsterdam, The Netherlands

† Homogeneous, Supramolecular & Bio-Inspired Catalysis van 't Hoff Institute for Molecular Sciences, University of Amsterdam, P.O. Box 94720, 1090 GE Amsterdam, the Netherlands

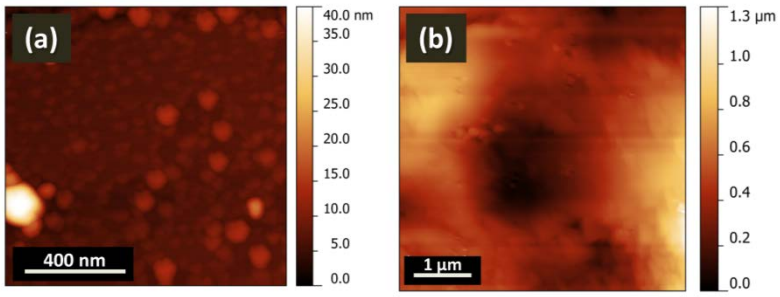

Figure S1. Comparison of the surface roughness of stamped and un-stamped $CH_3NH_3PbBr_3$ crystals. Atomic force microscopy image (AFM) of the surface of a crystal formed by spin coating (a) with and (b) without PDMS-stamping .

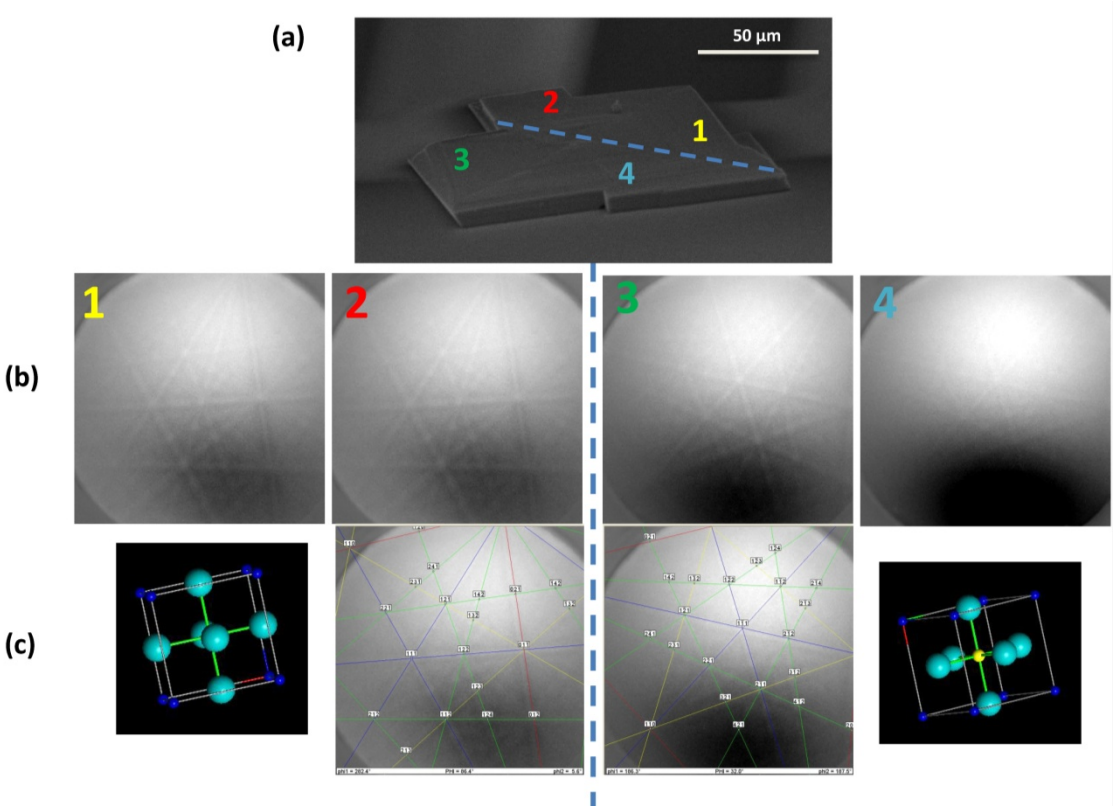

Figure S2. EBSD of a crystal with two domains. a) SEM image of the crystal of $CH_3NH_3PbBr_3$. Numbers show the position of the electron beam where the EBSD patterns were collected. The dashed line indicates the boundary between domains, based on the crystal's morphology and EBSD patterns. b) EBSD patterns from four different points. Patterns from each side of the dashed line are similar to each other but different from the patterns collected from the other side of the line. c) Indexed EBSD patterns and crystal orientation of $CH_3NH_3PbBr_3$, extracted from the indexed Kikuchi patterns. The crystal orientations of the patterns are <100> (left) and <110> (right). Green spheres are bromide anions, while blue spheres represent the methylammonium cations. The yellow sphere is the lead cation.

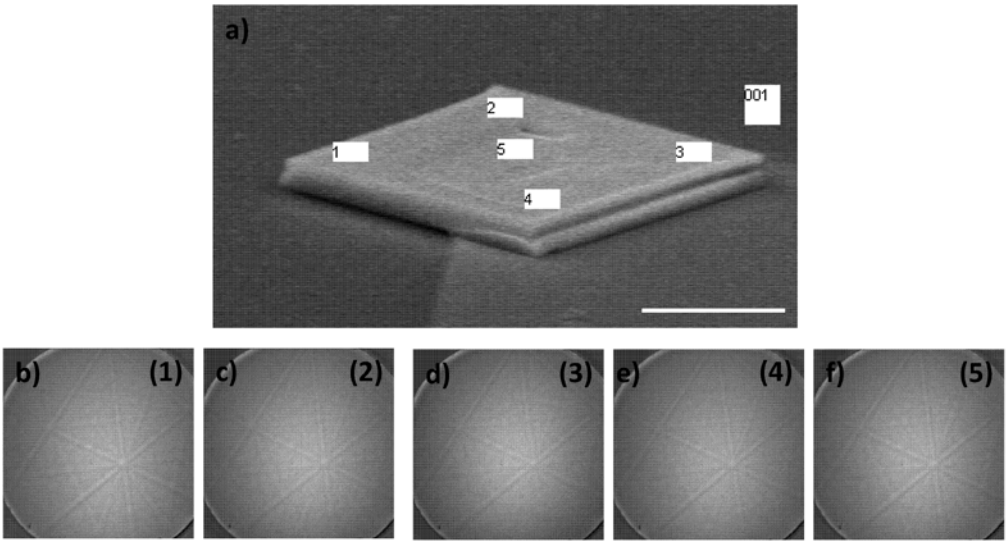

Figure S3. Electron backscatter diffraction (EBSD) of a $CsPbBr_3$ crystal. (a) SEM image of a $CsPbBr_3$ single crystal. Numbers indicate the positions of the electron beam where the EBSD patterns were collected. (b-f) EBSD patterns from locations 1-5 on the crystal, which all show the same Kikuchi pattern indicating the same crystallographic orientation.

Single crystal x-ray diffraction of $CH_3NH_3PbBr_3$

To confirm the single-crystalline character of the grown crystals, the unit cell parameters of several randomly selected crystals were measured using single crystal x-ray diffraction. In all cases the cubic unit cell was found (a = b = c = 5.92 Å), which is in accord with previous reports[1-3]. Solution of the crystal structure of one of the selected crystals confirmed the $Pm\bar{3}m$ space group (no. 221). As pointed out by Knop et al.[2] in this space group, the $CH_3NH_3^+$ cation has to be positionally disordered over at least 6 equivalent C–N orientations. This should also lead to a small intensity of diffraction compared to the contributions of Pb^{2+} and Br^-. Indeed, due to this disorder, determining the precise location of the N and C atoms was difficult; however, a model with the CH_3NH_3 cation being disordered over 12 positions led to a satisfactory R-value. The assignment of the N vs. C atoms was based on the expectation that the NH_3^+ group should be directed towards the negatively charged Br^- atom. During an unconstrained refinement, due to the positional disorder, the C and N atoms tended to shorten their distance to values close to 1 Å; therefore, their distance was constrained to 1.50 Å and these atoms were refined isotropically. As a result of the disorder, no satisfactory positioning of the hydrogen atoms of the CH_3NH_3 cation could be obtained, as after refinement they tended to occupy chemically wrong locations; therefore, for the final solution the hydrogen atoms were not included. The above results are in agreement with the structure recently reported by Shi et al.[3] (Figure S4).

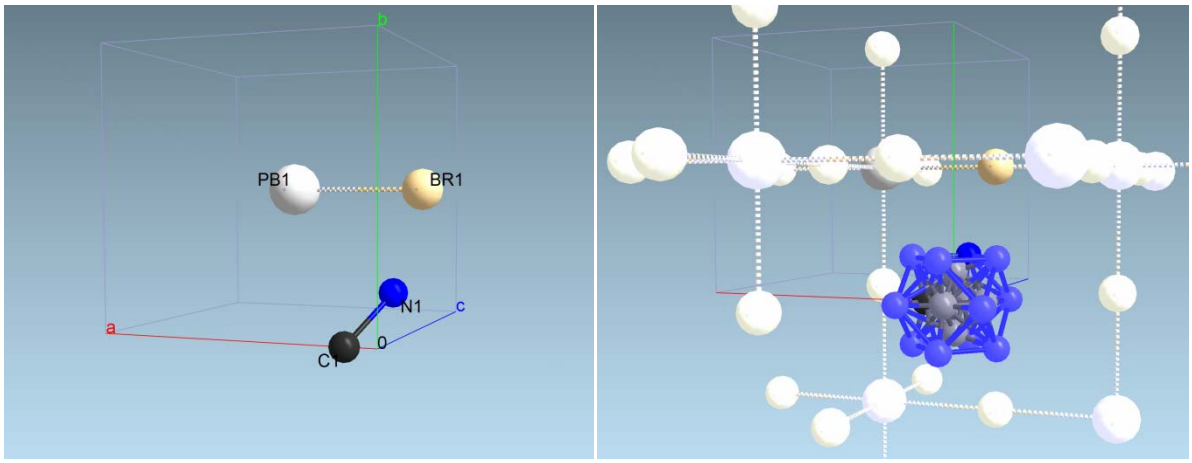

Figure S4. Asymmetric unit of $CH_3NH_3PbBr_3$ (left) and positional disorder of the $CH_3NH_3^+$ cation. Visualization was made with ShelXle.

Experimental methods of single crystal x-ray diffraction

Data was collected on a Bruker D8 Quest Eco diffractometer, equipped with a TRIUMPH monochromator and a CMOS PHOTON 50 detector, using Mo-Kα radiation (λ = 0.71073 Å). The intensity data were integrated with the Bruker APEX2 software [4]. Absorption correction and scaling was performed with SADABS[5]. The structures were solved with SHELXT. Least-squares refinement was performed with SHELXL-2014[6].

An intense orange plate-like specimen of $CH_3NH_3PbBr_3$, approximate dimensions 0.026 mm x 0.187 mm x 0.227 mm, was used for the x-ray crystallographic analysis. The x-ray intensity data were measured.

A total of 86 frames were collected. The total exposure time was 0.24 hours. The frames were integrated with the Bruker SAINT software package using a narrow-frame algorithm. The integration of the data using a cubic unit cell yielded a total of 496 reflections to a maximum θ angle of 26.16° (0.81 Å resolution), of which 68 were independent (average redundancy 7.294, completeness = 100.0%, R_{int} = 5.49%, R_{sig} = 3.85%) and 68 (100.00%) were greater than $2\sigma(F^2)$. The final cell constants of a = 5.9222(18) Å, b = 5.9222(18) Å, c = 5.9222(18) Å, volume = 207.71(19) $Å^3$, are based upon the refinement of the XYZ-centroids of 75 reflections above 20 σ(I) with 6.818° < 2θ < 52.30°. Data were corrected for absorption effects using the multi-scan method (SADABS). The ratio of minimum to maximum apparent transmission was 0.215. The calculated minimum and maximum transmission coefficients (based on crystal size) are 0.0470 and 0.1780.

The final anisotropic full-matrix least-squares refinement on F^2 with 9 variables converged at R1 = 3.52%, for the observed data and wR2 = 10.26% for all data. The goodness-of-fit was 1.349. The largest peak in the final difference electron density synthesis was 2.540 $e^-/Å^3$ and the largest hole was -1.561 $e^-/Å^3$ with an RMS deviation of 0.290 $e^-/Å^3$. On the basis of the final model, the calculated density was 3.829 g/cm^3 and F(000), 206 e^-.

Table 1. Single Crystal XRD Data of $CH_3NH_3PbBr_3$

Temperature	296 K	
Wavelength	0.71073 Å	
Crystal size	0.026 x 0.187 x 0.227 mm	
Crystal habit	intense orange plate	
Crystal system	cubic	
Space group	P m $\bar{3}$ m	
Unit cell dimensions	a = 5.9222(18) Å	α = 90°
	b = 5.9222(18) Å	β = 90°
	c = 5.9222(18) Å	γ = 90°
Volume	207.71(19) $Å^3$	
Z	1	
Density (calculated)	3.829 g/cm^3	
Absorption coefficient	34.633 mm^{-1}	
F(000)	206	

Table 2. Atomic coordinates and equivalent isotropic atomic displacement parameters ($Å^2$)

U(eq) is defined as one third of the trace of the orthogonalized U_{ij} tensor.

	x/a	**y/b**	**z/c**	**U(eq)**
Pb1	0.5	0.5	0.5	0.0254(11)
Br1	0.0	0.5	0.5	0.097(2)
C1	0.111(18)	0.0	0.0	0.010(19)

	x/a	y/b	z/c	U(eq)
N1	0.0	0.161(7)	0.161(7)	0.15(18)

Table 3. Bond lengths (Å)

Pb1-Br1	2.9611(9)	Pb1-Br1	2.9611(9)
Pb1-Br1	2.9611(9)	Pb1-Br1	2.9611(9)
Pb1-Br1	2.9611(9)	Pb1-Br1	2.9611(9)
Br1-Pb1	2.9611(9)	C1-C1	0.93(15)
C1-C1	0.93(15)	C1-C1	0.93(15)
C1-C1	0.93(15)	C1-N1	0.99(8)
C1-N1	0.99(8)	C1-N1	0.99(8)
C1-N1	0.99(8)	C1-C1	1.3(2)
C1-N1	1.50(2)	C1-N1	1.50(2)
C1-N1	1.50(2)	N1-C1	0.99(8)
N1-C1	0.99(8)	N1-N1	1.34(6)
N1-N1	1.34(6)	N1-N1	1.34(6)
N1-N1	1.34(6)	N1-C1	1.50(2)
N1-C1	1.87(5)	N1-C1	1.87(5)

Table 4. Bond angles (°)

Br1-Pb1-Br1	90.0	Br1-Pb1-Br1	90.0
Br1-Pb1-Br1	180.0	Br1-Pb1-Br1	90.0
Br1-Pb1-Br1	90.0	Br1-Pb1-Br1	90.0
Br1-Pb1-Br1	90.0	Br1-Pb1-Br1	90.0

Br1-Pb1-Br1	90.0	Br1-Pb1-Br1	180.0
Br1-Pb1-Br1	180.0	Br1-Pb1-Br1	90.0
Br1-Pb1-Br1	90.0	Br1-Pb1-Br1	90.0
Br1-Pb1-Br1	90.0	Pb1-Br1-Pb1	180.0
C1-C1-C1	60.0	C1-C1-C1	90.000(4)
C1-C1-C1	60.000(4)	C1-C1-C1	60.000(4)
C1-C1-C1	90.000(4)	C1-C1-C1	60.0
C1-C1-N1	152.(7)	C1-C1-N1	102.(5)
C1-C1-N1	62.(7)	C1-C1-N1	102.(5)
C1-C1-N1	102.(5)	C1-C1-N1	152.(7)
C1-C1-N1	102.(5)	C1-C1-N1	62.(7)
N1-C1-N1	85.(4)	C1-C1-N1	102.(5)
C1-C1-N1	62.(7)	C1-C1-N1	102.(5)
C1-C1-N1	152.(7)	N1-C1-N1	85.(4)
N1-C1-N1	146.(10)	C1-C1-N1	62.(7)
C1-C1-N1	102.(5)	C1-C1-N1	152.(7)
C1-C1-N1	102.(5)	N1-C1-N1	146.(10)
N1-C1-N1	85.(4)	N1-C1-N1	85.(4)
C1-C1-C1	45.0	C1-C1-C1	45.0
C1-C1-C1	45.0	C1-C1-C1	45.0
N1-C1-C1	107.(7)	N1-C1-C1	107.(7)
N1-C1-C1	107.(7)	N1-C1-C1	107.(7)
C1-C1-N1	40.(3)	C1-C1-N1	40.(3)
C1-C1-N1	98.(4)	C1-C1-N1	98.(4)

N1-C1-N1	137.(3)	N1-C1-N1	137.(3)
N1-C1-N1	61.(2)	N1-C1-N1	61.(2)
C1-C1-N1	64.(4)	C1-C1-N1	98.(4)
C1-C1-N1	98.(4)	C1-C1-N1	40.(3)
C1-C1-N1	40.(3)	N1-C1-N1	61.(2)
N1-C1-N1	61.(2)	N1-C1-N1	137.(3)
N1-C1-N1	137.(3)	C1-C1-N1	64.(4)
N1-C1-N1	128.(9)	C1-C1-N1	40.(3)
C1-C1-N1	98.(4)	C1-C1-N1	98.(4)
C1-C1-N1	40.(3)	N1-C1-N1	137.(3)
N1-C1-N1	61.(2)	N1-C1-N1	137.(3)
N1-C1-N1	61.(2)	C1-C1-N1	64.(4)
N1-C1-N1	79.(4)	N1-C1-N1	79.(4)
C1-N1-C1	56.(10)	C1-N1-N1	47.(2)
C1-N1-N1	78.(5)	C1-N1-N1	78.(5)
C1-N1-N1	47.(2)	N1-N1-N1	60.000(3)
C1-N1-N1	47.(2)	C1-N1-N1	78.(5)
N1-N1-N1	90.0	N1-N1-N1	120.0
C1-N1-N1	78.(5)	C1-N1-N1	47.(2)
N1-N1-N1	120.000(2)	N1-N1-N1	90.000(2)
N1-N1-N1	60.000(2)	C1-N1-C1	38.(8)
C1-N1-C1	38.(8)	N1-N1-C1	40.(3)
N1-N1-C1	40.(3)	N1-N1-C1	82.(4)
N1-N1-C1	82.(4)	C1-N1-C1	38.(8)

C1-N1-C1	38.(8)	N1-N1-C1	82.(4)
N1-N1-C1	82.(4)	N1-N1-C1	40.(3)
N1-N1-C1	40.(3)	C1-N1-C1	52.(9)
C1-N1-C1	14.(5)	C1-N1-C1	42.(9)
N1-N1-C1	52.5(9)	N1-N1-C1	68.9(13)
N1-N1-C1	52.5(9)	N1-N1-C1	68.9(13)
C1-N1-C1	30.(5)	C1-N1-C1	30.(5)
C1-N1-C1	42.(9)	C1-N1-C1	14.(5)
N1-N1-C1	68.9(13)	N1-N1-C1	52.5(9)
N1-N1-C1	68.9(13)	N1-N1-C1	52.5(9)
C1-N1-C1	30.(5)	C1-N1-C1	30.(5)
C1-N1-C1	29.(4)		

Table 5. Anisotropic atomic displacement parameters (Å^2)

The anisotropic atomic displacement factor exponent takes the form: $-2\pi^2[h^2 a^{*2} U_{11} + ... + 2 h k a^* b^* U_{12}]$

	U_{11}	U_{22}	U_{33}	U_{23}	U_{13}	U_{12}
Pb1	0.0254(11)	0.0254(11)	0.0254(11)	0	0	0
Br1	0.021(2)	0.136(4)	0.136(4)	0	0	0

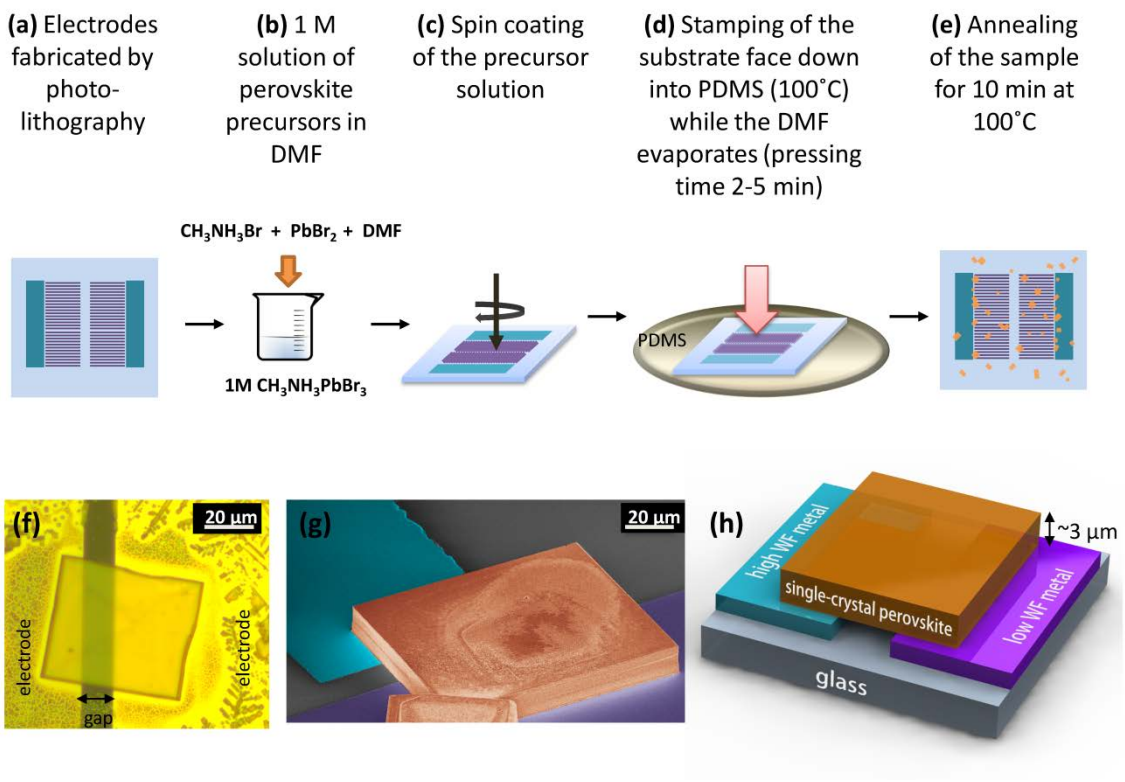

Figure S5. Perovskite solar cells fabricated using the back-contacted device platform. (a) A glass substrate with electrodes fabricated using two steps of photolithography. (b) 1 M solution of the precursors, CH_3NH_3Br and $PbBr_2$,in DMF. (c) Spin-coating of the solution on top of the prepared electrodes. The solvent was not allowed to evaporate fully. (d) Pressing the substrate face down into PDMS on a hotplate (100°C) until the crystals formed. (e) Schematic of the final sample with crystals distributed randomly over the substrate after annealing it face up for an additional 10 minutes. Some of the crystals bridged the gaps between the electrodes to form devices. (f) Optical microscopy image of a $CH_3NH_3PbBr_3$ single crystal formed in the gap between two pre-fabricated electrodes. (g) False-color SEM image of a single crystal of $CH_3NH_3PbBr_3$ (orange) bridging the gap between two electrodes (blue for titanium, purple for palladium). (h) Schematic of a microscale perovskite solar cell made with high and low work function (WF) metals as carrier-selective contacts.

Materials selection for the electrodes of the back-contacted platform

In order to make solar cells, the electrodes were fabricated on glass substrates using two steps of photolithography prior to the deposition of the perovskite crystals (as explained in the experimental section). Because the electrodes are fabricated before deposition of the crystals, this platform avoids the difficulty of finding a process for layer deposition that will not damage the perovskite. Standard processes for thin-film deposition – such as those requiring high temperature, plasma, incompatible solvents (e.g water), or oxidizing environments – can be used to fabricate the underlying contacts. Also, if no surface reactions occur between the electrodes and the perovskite, this structure is also a reusable test platform because the crystals can be removed using a suitable solvent. After the solution deposition and PDMS stamping, crystals were distributed randomly on the substrate so that some bridged the gaps

between the electrodes (Figure S5). The large size of the crystals, whose edges often exceed 50 µm, enables optical imaging and facilitates in-situ characterization of the devices. In order to choose the correct carrier-selective electrode for $CH_3NH_3PbBr_3$ back-contacted devices, a list of metals with higher work function than the valance band and lower work function than the conduction band of $CH_3NH_3PbBr_3$ was considered (Figure S6). The first requirement for selecting the electrode material is chemical stability of the electrode in the perovskite precursor solution. Ti electrodes were stable upon the deposition of the perovskite solution. When the $CH_3NH_3PbBr_3$ devices with symmetric electrodes (Ti-Ti) were fabricated, they had linear *I-V* curves, indicating the ohmic nature of the contact (Figure S6). Other metals with similarly small work functions, such as aluminum and silver, were also tested; however, severe corrosion of the metal was observed immediately following deposition of the perovskite solution.

Devices with Pd-Pd contacts were fabricated to test Pd as a hole-selective electrode for $CH_3NH_3PbBr_3$ solar cell devices. They were stable and conductive but showed saturation in their current (Figure S6). While the cause of this saturation is unknown, similar behavior arises in other semiconductors when scattering with phonons or impurities imposes a limit on the drift velocity of the carriers at high fields. Alternatively, saturation can also appear when the conduction channel of the device becomes restricted, as is the case in transistors [7]. Gold and nickel were also tested as hole-selective electrodes; however, the devices with Au-Au electrodes did not show stable *I-V* behavior (Figure S7). In the case of devices with symmetric Ni-Ni electrodes, although no damage to the electrodes was visible after deposition of the perovskite crystals, running current through the devices caused them to break down electrically, and the appearance of the nickel electrode was altered. Energy-dispersive x-ray spectroscopy (EDS) confirmed the loss of nickel atoms from the electrode near the $CH_3NH_3PbBr_3$ crystal (Figure S6). Platinum was also tested for the hole-selective contact and showed behavior similar to that of palladium (Figure S8).

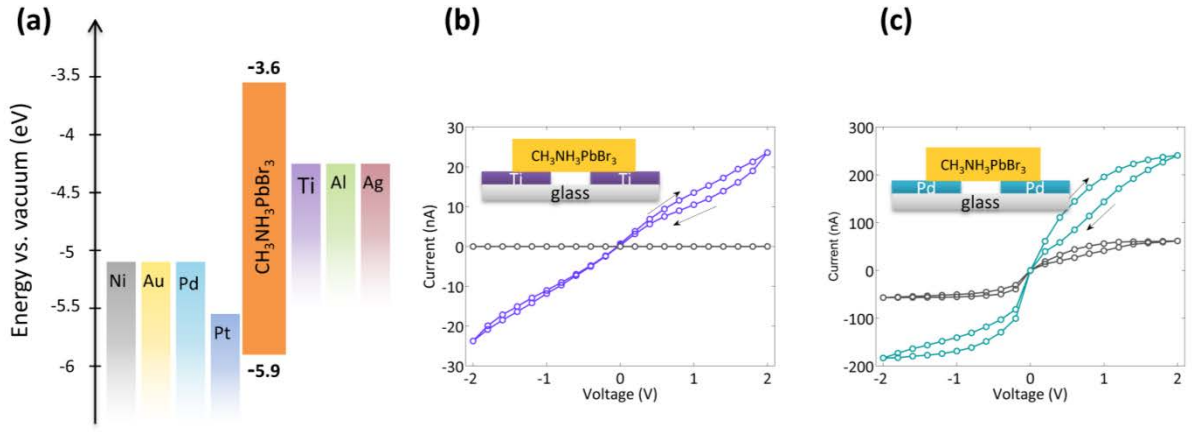

Figure S6. Electrical characterization of $CH_3NH_3PbBr_3$ single crystals using the symmetric back-contacted device platform (a) Energy band diagram for $CH_3NH_3PbBr_3$ [8] and metals with appropriate work functions for extracting holes and electrons. (b) I-V curves of $CH_3NH_3PbBr_3$ single crystals in the dark (gray) and under 1-sun illumination (colors) with symmetric electron-selective electrodes (Ti-Ti) and (c) symmetric hole-selective electrodes (Pd-Pd).

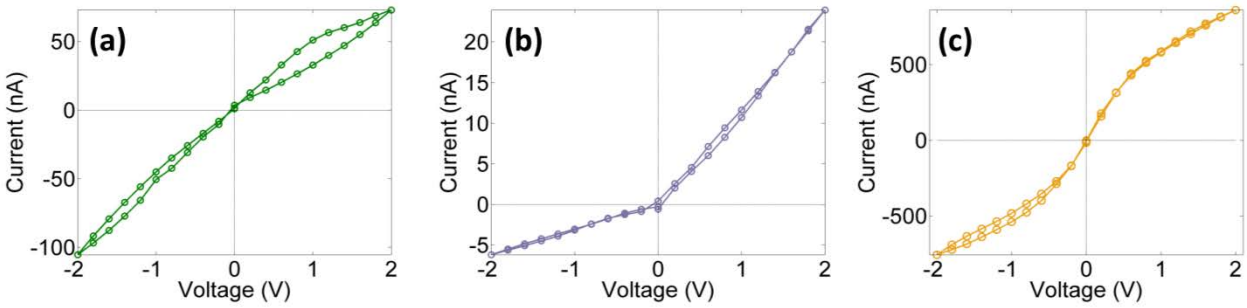

Figure S7. Testing other high work function metals (gold and platinum) as hole-selective electrodes. *I-V* characteristics of $CH_3NH_3PbBr_3$ crystals with (a-b) Au-Au and (c) Pt-Pt symmetric electrodes under 1-sun illumination. Au-Au electrodes did not have stable *I-V* curves over repeated measurements, as these *I-V* curves are from the same crystal at different times. Pt-Pt devices had stable and symmetric *I-V* characteristics, but use of Pt was discontinued because of practical difficulties in e-beam evaporating Pt.

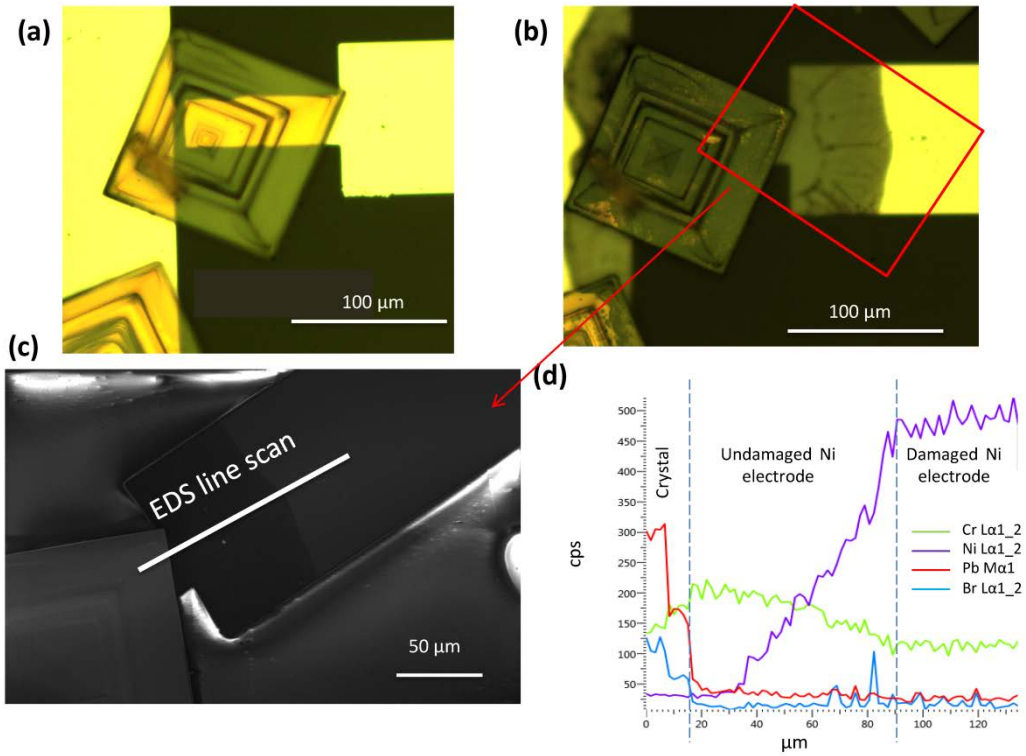

Figure S8. Reactivity of symmetric Ni-Ni electrodes. A $CH_3NH_3PbBr_3$ crystal on top of the electrodes before (a) and after (b) running current through the device. (c) SEM image of the damaged part is shown in which an energy-dispersive x-ray spectroscopy (EDS) line scan was performed. (d) The EDS spectrum indicates the loss of Ni from the electrode near the crystal.

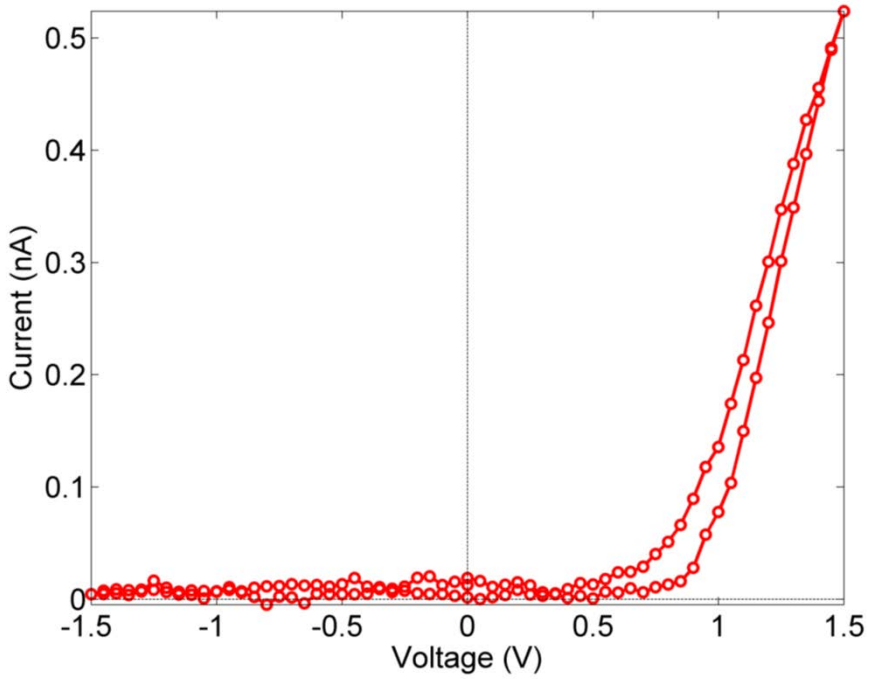

Figure S9. ***I-V*** **curve of the back-contacted $CH_3NH_3PbBr_3$ single crystal presented in figure 3 under the dark condition.**

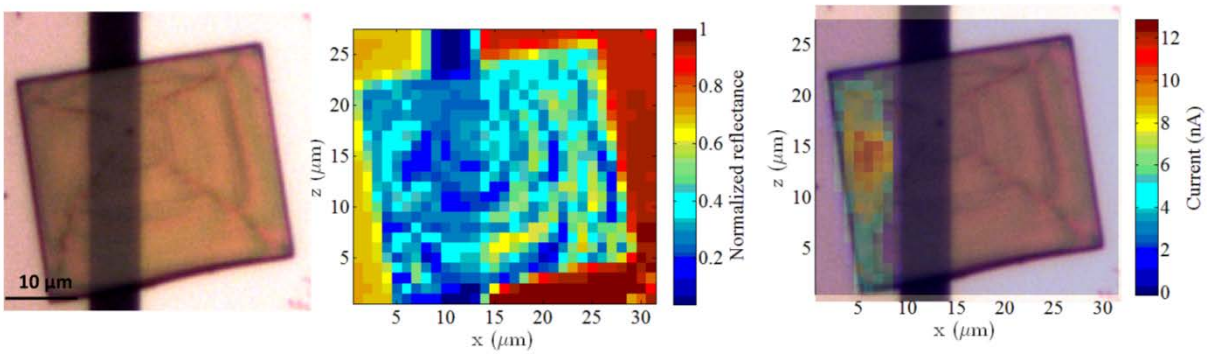

Figure S10. Superimposed optical image and photocurrent map of the $CH_3NH_3PbBr_3$ single crystal presented in figure 3d. It shows that the photocurrent is produced only directly above the Ti electrode, which is the electron-selective contact.

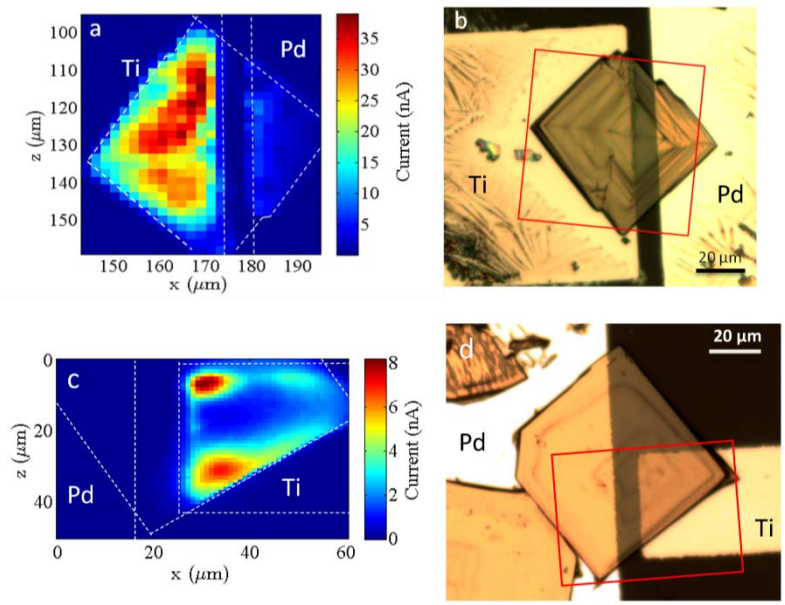

Figure S11. Scanning photocurrent maps (a and c) and optical images (b and d) of two different back-contacted $CH_3NH_3PbBr_3$ single crystals. The red squares define where the photocurrent was mapped. These maps, along with the third presented in the main text, show that the hot spots in the photocurrent vary in their positions with different devices.

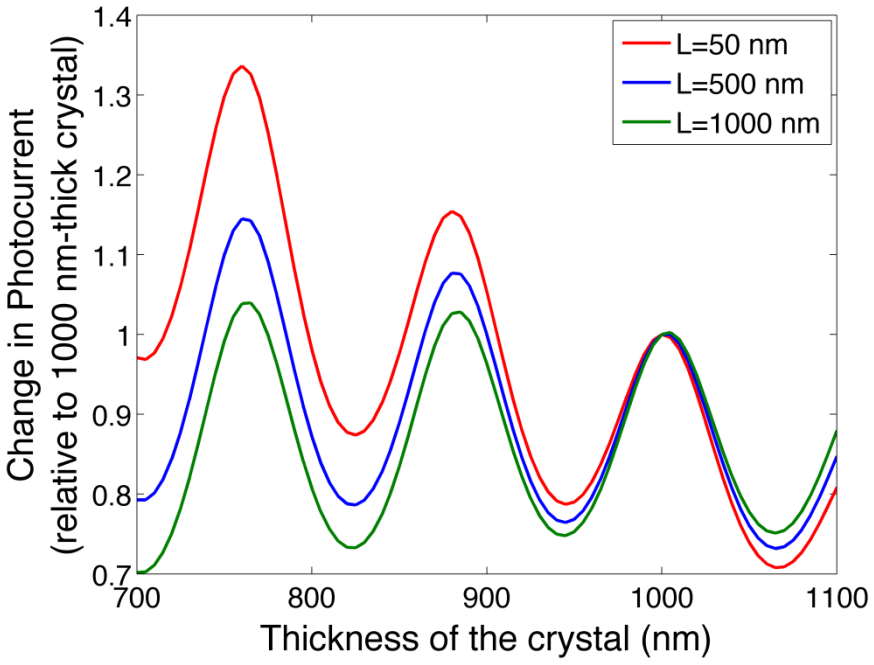

Figure S12. Calculation of the relative change in photocurrent (at λ =540 nm) expected with changes in the thickness of the crystal. Changes are estimated relative to a 1000-nm-thick crystal and for three different diffusion lengths (L). A thickness variation in the crystal can cause both increases and decreases in photocurrent, but the total magnitude of the change (from minimum to maximum) is always less than a factor of two.

In general, the photocurrent I at a particular wavelength in a crystal of thickness d is given by:

$$I = \int_0^d G(x)C(x)dx$$

where *G(x)*, is the generation profile as a function of depth (*x*), and is calculated numerically using a transfer-matrix model that accounts for thin-film interference and back reflection from the Ti electrode.[9] Values of the refractive indices for the perovskite[10] and Ti[11] were taken from the literature. The refractive index of the SiO_2 was measured by ellipsometry. The collection efficiency was modeled as an exponential decay from the perovskite-electrode interface:

$$C(x) = C_0 e^{(x-d)/L}$$

in which C_0 is a constant that describes the collection efficiency at the perovskite-metal interface, *d* is the thickness of the crystal, and *L* is the minority carrier diffusion length.

Based on this calculation, the changes in photocurrent in the map of the main text (a factor of four increase) cannot arise solely from a local change in the crystal's thickness (*d*), assuming that the local collection efficiency at the contact (C_0) and diffusion length (*L*) remain constant. AFM (**Figure S13**) shows that the crystal's thickness over the Ti electrode varies in the simulated range, from 760 to 1000 nm.

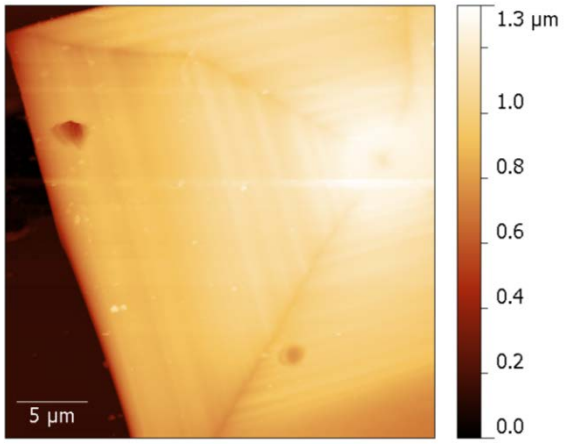

Figure S13. Atomic force microscopy of the $CH_3NH_3PbBr_3$ single crystal device presented in figure 3

References

[1] D. Weber, *Zeitschrift für Naturforschung B*, **1978**, *33*, 1443.

[2] O. Knop, R. E. Wasylishen, M. A. White, T. S. Cameron and M. J. M. V. Oort, *Can. J. Chem.*, **1990**, *68*, 412-422.

[3] D. Shi, V. Adinolfi, R. Comin, M. Yuan, E. Alarousu, A. Buin, Y. Chen, S. Hoogland, A. Rothenberger, K. Katsiev, Y. Losovyj, X. Zhang, P. A. Dowben, O. F. Mohammed, E. H. Sargent and O. M. Bakr, *Science*, **2015**, *347*, 519-522.

[4] Bruker, *Madison, WI, USA, 2014*.

[5] G. M. Sheldrick, SADABS: Area-Detector Absorption Correction. *Universität Göttingen, Germany*, **1999**

[6] G. M. Sheldrick, SHELXT. *Universität Göttingen, Germany*, **2012**.

[7] S. M. Sze and K. K. Ng, *Physics of semiconductor devices*, John Wiley & Sons, Inc., Hoboken, New Jersey, **2007**.

[8] A. Goldmann, H. Landolt and R. Börnstein, *Electronic structure of solids: Photoemission spectra and related data*, Springer, New York, **1994**.

[9] G. F. Burkhard, E. T. Hoke, M. D. McGehee, *Adv. Mater.* **2010**, 22, 3293-3297.

[10] Brittman, S.; Garnett, E. C., Measuringnandkat the Microscale in Single Crystals of Ch3nh3pbbr3perovskite. The Journal of Physical Chemistry C 2016, 120, 616-620.

[11] D. W. Lynch, C. G. Olson, and J. H. Weaver. *Phys. Rev. B* **1975**, 11, 3617-3624.